

Article

A MIM Waveguide Structure of a High-Performance Refractive Index and Temperature Sensor Based on Fano Resonance

Pengwei Liu ^{1,2,3} , Shubin Yan ^{2,3,*} , Yifeng Ren ¹, Xiaoyu Zhang ¹, Tingsong Li ¹, Xiushan Wu ², Lifang Shen ² and Ertian Hua ²

¹ School of Electrical and Control Engineering, North University of China, Taiyuan 030051, China; lpw18834800530@163.com (P.L.); Renyifeng126@126.com (Y.R.); zhangxiaoyu9725@163.com (X.Z.); lts15296737639@163.com (T.L.)

² School of Electrical Engineering, Zhejiang University of Water Resources and Electric Power, Hangzhou 310018, China; wuxs@zjweu.edu.cn (X.W.); shenlf@zjweu.edu.cn (L.S.); het@zjut.edu.cn (E.H.)

³ Joint Laboratory of Intelligent Equipment and System for Water Conservancy and Hydropower Safety Monitoring of Zhejiang Province and Belarus, Hangzhou 310018, China

* Correspondence: yanshb@zjweu.edu.cn; Tel.: +86-186-3611-2255

Abstract: A plasmonic refractive index nanosensor structure consisting of a metal-insulator-metal (MIM) waveguide with two symmetrical rectangle baffles coupled with a connected-concentric-double rings resonator (CCDRR) is presented. In this study, its transmission characteristics were investigated using the finite element method (FEM). The consequences, studied via simulation, revealed that the transmission spectrum of the system presents a sharp asymmetric Fano profile due to the destructive interference between the wide-band mode of two rectangle baffles on the bus waveguide and the narrow-band mode of the CCDRR. The effects of the geometric parameters of the structure on the transmission characteristics were investigated comprehensively. A sensitivity of 2260 nm/RIU and figure of merit (FOM) of 56.5 were the best levels of performance that the designed structure could achieve. In addition, the system could act as a sensor for use for temperature sensing, with a sensitivity that could reach 1.48 nm/°C. The designed structure advances with technology with new detection positions and has good application prospects in other high-sensitivity nanosensor fields, for example, acting as a biosensor to detect the hemoglobin level in the blood.

Keywords: plasmonic refractive-index nanosensor; Fano resonance; metal-insulator-metal waveguide; temperature sensor



check for updates

Citation: Liu, P.; Yan, S.; Ren, Y.; Zhang, X.; Li, T.; Wu, X.; Shen, L.; Hua, E. A MIM Waveguide Structure of a High-Performance Refractive Index and Temperature Sensor Based on Fano Resonance. *Appl. Sci.* **2021**, *11*, 10629. <https://doi.org/10.3390/app112210629>

Academic Editor: Agnese Magnani

Received: 14 October 2021

Accepted: 4 November 2021

Published: 11 November 2021

Publisher's Note: MDPI stays neutral with regard to jurisdictional claims in published maps and institutional affiliations.



Copyright: © 2021 by the authors. Licensee MDPI, Basel, Switzerland. This article is an open access article distributed under the terms and conditions of the Creative Commons Attribution (CC BY) license (<https://creativecommons.org/licenses/by/4.0/>).

1. Introduction

Surface plasmon polaritons (SPPs) is a phenomenon whereby a metal surface charges when interacting with a light wave electromagnetic field; they oscillate collectively, so that the electromagnetic field is limited to a small range and is enhanced [1]. SPPs cannot only break through the diffraction limit of light, but is also highly sensitive to metal types, the dielectric environment, nano-shape, and size [2]. Hence, photonic devices designed based on SPPs cannot only realize the integration of the sub-wavelength size [3–5], but also provide the possibility of studying micro-nanophotonic devices with complex functions. It is worth mentioning that many optical phenomena have been observed in the plasmon waveguide coupling system, such as phase-coupled plasmon-induced transparency [6] and Fano resonance [7–9]. Fano resonance generally comes from the destructive interference between the wide-band mode (bright mode) and the narrow-band mode (dark mode) in plasmon resonance, which has a small radiation loss, a narrow full width at half maximum (FWHM), and an asymmetric spectral line shape [10,11]. Therefore, it has great application potential in refractive index sensors [12,13], slow light devices [14], and optical switches [15].

Nowadays, many waveguide coupling structures based on SPPs have been designed to fabricate various photonic devices, including metal–insulator–metal (MIM) waveguides [16], insulator–metal–insulator waveguides [17], channel waveguides [18,19], and nanoparticle chain waveguides [20]. Among them, MIM waveguides are widely considered and reported by scholars and the media at home and abroad because of their sub-wavelength size, simple structure, easy integration, and high reliability [16,21]. Yang et al. [22] designed a coupling structure with a double-gap ring cavity and MIM waveguides with two triangular baffles with a sensitivity of 1500 nm/RIU and figure of merit (FOM) of 65.2. Tang et al. [23] proposed and studied a plasmonic structure that includes a ring nanocavity, two bus waveguides, and a rectangular nanocavity, with a sensitivity of 1125 nm/RIU. Su et al. [24] devised a plasmonic sensor coupled with an elliptical ring cavity and a MIM waveguide with two rectangle baffles; its sensitivity is 1550 nm/RIU and FOM is 43.05. As shown in Table 1, although the difference of FOM is not obvious, the sensitivity of the designed structure is obviously better than that of other structures. In addition, various photonic devices based on MIM waveguide structure design, such as optical splitters [25,26], filters [27,28], and Bragg reflectors [29,30], have achieved remarkable results.

Table 1. Performance comparison of various plasmonic sensors.

| Reference | Sensitivity (nm/RIU) | FOM |
|------------------|----------------------|-------|
| This work | 2260 | 56.5 |
| Yang et al. [22] | 1500 | 65.2 |
| Tang et al. [23] | 1125 | 75 |
| Su et al. [24] | 1550 | 43.05 |

Herein, a plasmonic structure consisting of a MIM waveguide with two symmetrical rectangle baffles coupled with a connected concentric double rings resonator (CCDRR) is presented and investigated. The transmission characteristics and the normalized magnetic field distribution were calculated, introducing the finite element method (FEM). In addition to the influence of the refractive-index of the dielectric on the transmission characteristics of Fano resonance, the influence of the geometric parameters of the structure was also studied. These parameters include the external radii of the outer ring and inner ring of the CCDRR, the separation between the two symmetrical rectangular baffles, the heights of the two rectangular baffles, and the coupling gap between the CCDRR and the bus waveguide. Additionally, applications of the designed structure in refractive-index sensing and temperature sensing were studied in detail. The designed structure provides new detection positions, which may be helpful for meeting special requirements for detection wavelengths.

2. Structural Model and Analysis Methods

A schematic diagram of the presented MIM bus waveguide coupled with two rectangular baffles and a CCDRR is displayed in Figure 1. The width w of the MIM waveguide, two rectangular baffles, and two annulus cavities remained invariable at 50 nm to ensure that the waveguide only supports the transverse magnetic field (TM_0) mode. g represents the coupling gap between the bus waveguide and the CCDRR. The heights of the two rectangle baffles and the separation between them are signified as h and H , respectively. R_1 and r_1 , R_2 and r_2 express the external and internal radii of the outer ring and inner ring, respectively. d is defined as the width of the baffles connecting two rings in the concentric ring, which is fixed at 40 nm.

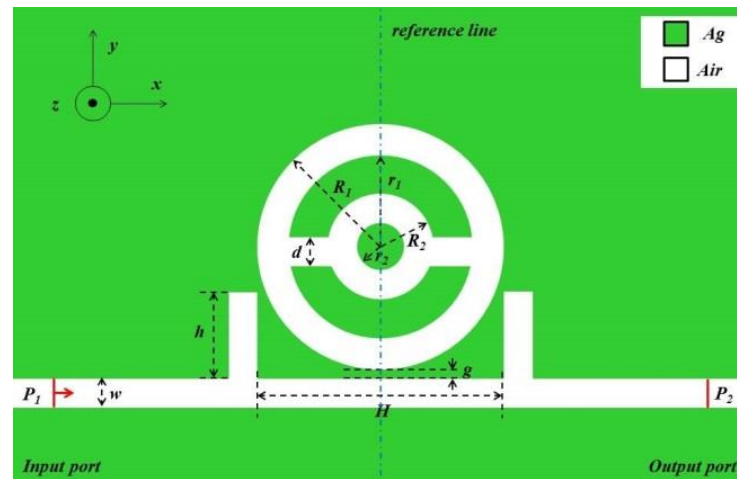


Figure 1. Two-dimensional schematic diagram of a metal–insulator–metal (MIM) waveguide with twin symmetrical rectangle baffles coupled with a connected concentric double rings resonator (CCDRR).

The white part and green part in Figure 1 represent air and silver, respectively. The relative permittivity ϵ_d of air is 1. Based on the Debye–Drude dispersion model [31], the description of the relative dielectric constant of Ag is as follows:

$$\epsilon(\omega) = \epsilon_\infty + \frac{\epsilon_s - \epsilon_\infty}{1 + i\omega\tau} + \frac{\sigma}{i\omega\epsilon_0} \tag{1}$$

where $\epsilon_\infty = 3.8344$ is the boundless frequency dielectric constant and $\epsilon_s = -9530.5$ is the static dielectric constant. The relaxation time and the conductivity of Ag are regarded as $\tau = 7.35 \times 10^{-15}$ s and $\sigma = 1.1486 \times 10^7$ S/m, respectively.

The formula of the TM_0 mode of the MIM waveguide is as follows [32]:

$$\tanh(kw) = -\frac{2kp\alpha_c}{k^2 + p^2\alpha_c^2} \tag{2}$$

where $k = 2\pi/\lambda$ expresses the wave vector in the waveguide, and in free-space, k is taken as $k_0 = 2\pi/\lambda_0$; $\alpha_c = \sqrt{k_0^2(\epsilon_{in} - \epsilon_m) + k^2}$ and $p = \epsilon_{in}/\epsilon_m$; among them, ϵ_{in} and ϵ_m are the permittivity of the insulator and metal, respectively.

By analyzing the shifts of the Fano resonance wavelength, the sensing performance of the proposed structure in the waveguide coupled system was investigated. The transmission wavelengths and the effective refractive index's real part in the MIM waveguide can be expressed on the foundation of the standing wave theory as follows [33,34]:

$$\lambda_m = \frac{2\text{Re}(n_{eff})L}{m - \frac{\Psi_r}{\pi}} \quad (m = 1, 2, \dots) \tag{3}$$

$$\text{Re}(n_{eff}) = \sqrt{\epsilon_m + \left(\frac{k}{k_0}\right)^2} \tag{4}$$

where L indicates the circumference of the ring cavity; Ψ_r signifies the phase shift caused by the reflection of SPPs at the metal–insulator boundary surface; and m is a positive integral number, i.e., the number of antinodes of SPPs.

The characteristics of the sensor can be evaluated by two important parameters, namely, sensitivity (S) and FOM, which are expressed by the following equation [35]:

$$S = \frac{\Delta\lambda}{\Delta n} \tag{5}$$

$$FOM = \frac{S}{FWHM} \quad (6)$$

where $\Delta\lambda$ and Δn are the variation of resonant wavelength and refractive index, respectively.

In the next part of the paper, a simulation was run using COMSOL Multiphysics 5.4a. With the comparability of the operating principle of the two-dimensional (2D) mode and three-dimensional (3D) mode, a 2D geometric model with greatly reduced computational complexity was established, and the finite element method (FEM) was used to analyze the propagation characteristics. Then, hyperfine meshing was used to guarantee the accuracy of the emulation. In addition, the absorbing boundary condition was established by the perfect matched layer, which can absorb the outward reflected waves.

3. Simulations and Results

When comparing the performance of the double-ring cavity and the CCDRR, it was found that their sensitivity was almost the same in the range of the agreed refractive index change, but that the CCDRR had a higher FOM, so the CCDRR was chosen for further study.

To gain a distinct understanding of the propagation characteristics of the proposed structure, it was necessary to compare the whole system with the single CCDRR structure and the unitary two rectangular baffle structure. The unitary two rectangular baffle structure and the unitary CCDRR structure are shown in Figure 2a,b, respectively. The transmission spectra of the three structures are shown in Figure 2c. The geometric parameter settings are as follows: $R_1 = 190$ nm, $R_2 = 130$ nm, $H = 540$ nm, $h = 150$ nm, and $g = 10$ nm. The transmission spectra of the unitary two rectangular baffle structure, the unitary CCDRR structure, and the whole system are represented by the black, red, and blue solid lines, respectively. In Figure 2c, the black solid line representing the unitary two rectangular baffle structure has a positive slope, and it has relatively high transmittance in the range of 0.35 to 0.6. Hence, it can be regarded as a continuous wide-band mode. The transmission spectrum of the unitary CCDRR structure approximates the Lorentz line, which is considered as representing the discrete narrowband mode. It is obvious that the transmission spectrum of the whole structure (blue line) has an asymmetric shape, which indicates that Fano resonance is generated by the interaction of the successive wide-band mode and discrete narrow-band mode.

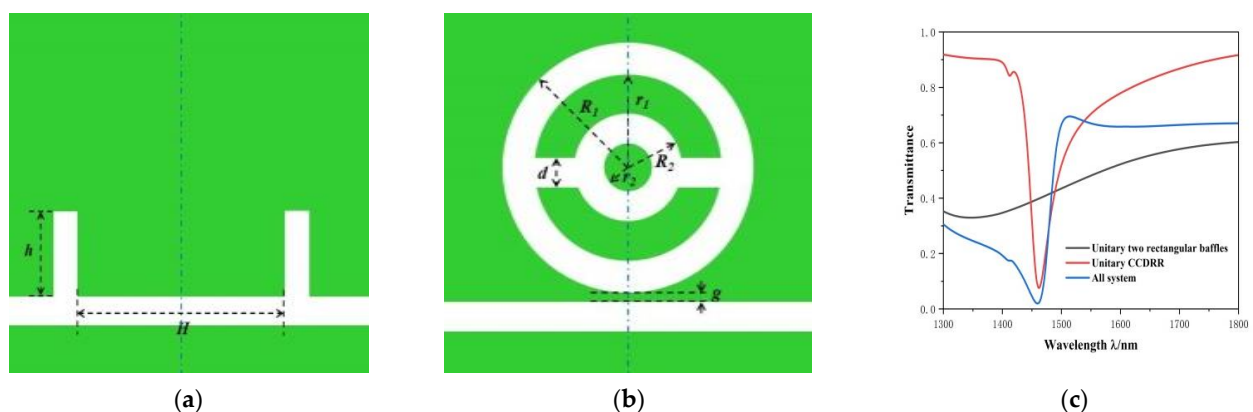


Figure 2. (a) Two-dimensional schematic diagram of the unitary two rectangular baffle structure; (b) 2D schematic diagram of the unitary CCDRR structure; and (c) the transmission spectrum of the unitary two rectangular baffle structure (black line), the unitary CCDRR structure (red line), and the whole system (blue line).

To better comprehend the inner theory of the black line's role in the Fano resonance of the whole structure, the magnetic field distributions and the electric field distributions of the unitary two rectangular baffles and the whole system at the resonance dip point ($\lambda = 1459$ nm) were demonstrated, which are shown in Figure 3a–d, respectively. In Figure 3a, there is a distinct resonance in the MIM waveguide, with only one bus wave-

uide and two rectangular baffles. As shown in Figure 3b, for the whole structure, the firm resonance occurs only on the left side, while infirm resonance occurs on the right. Additionally, the upper and lower parts of the outer ring in the CCDRR are anti-phase. Figure 3b,c provides insight into the actual energy distribution in the waveguides and the CCDRR cavity. In Figure 3c, there is an obvious energy distribution in the MIM waveguide. However, as shown in Figure 3d, the energy of SPPs is intensified at the CCDRR cavity and decreased at the right side of the waveguide. It was found that SPPs was directly coupled to the unitary two rectangular baffle structure and stimulated the resonance corresponding to the successive wide-band state, while the discrete narrow-band state in the CCDRR was indirectly stimulated by the SPPs in the two symmetrical rectangular baffles. Thus, the interaction of the two states produced the Fano resonance.

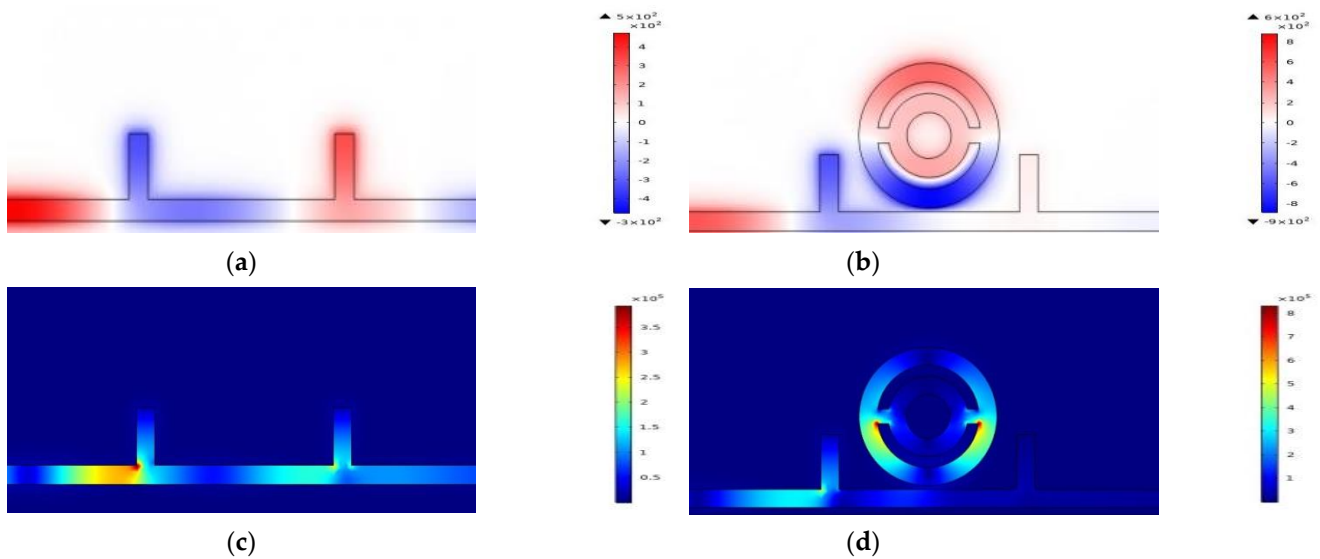


Figure 3. Normalized H_z field distributions at $\lambda = 1459$ nm of: (a) the unitary two rectangular baffles; (b) the whole structure; electric field distributions at $\lambda = 1459$ nm of: (c) the unitary two rectangular baffles; (d) the whole structure.

For further investigation of the influences of the different refractive indexes (n) on the transmission spectrum of the Fano resonance, six refractive indexes were simulated: 1.00, 1.01, 1.02, 1.03, 1.04, and 1.05 RIU. The structural arguments were as follows: $R_1 = 240$ nm, $R_2 = 130$ nm, $H = 540$ nm, $h = 150$ nm, and $g = 10$ nm. Figure 4a,b shows the simulation results. In Figure 4a, with the increase of n , the transmission spectra have an approximately equidistant red-shift. As shown in Figure 4b, when the refractive index changes, the change of dip wavelength-shift is linear. Therefore, the sensitivity of the sensor, which was 2260 nm/RIU with a FOM of 56.5, could be obtained from the slope after linear fitting, leading us to obtain the best result for the optimal parameter of the structure.

To investigate the influences of different external radii of the outer ring of the CCDRR on Fano resonance, R_1 was set to increase from 200 nm to 240 nm at an interval of 10 nm, while keeping other arguments fixed at $R_2 = 110$ nm, $H = 540$ nm, $h = 150$ nm, and $g = 10$ nm. The transmission spectra are displayed in Figure 5a. With the increase of R_1 , there is an obvious red shift at the dip point of Fano resonance, and the transmittance of this position increases slightly. The simulation result shows that R_1 determines the dip wavelength of Fano resonance. This phenomenon can be explained in other words as a scenario where the dip wavelength depends on the CCDRR corresponding to the narrowband pattern, with R_1 as an important parameter of the CCDRR. As shown in Figure 5b, by linear fitting, five solid lines representing the sensitivities of the different structures were obtained. As the external radius R_1 of the outer ring increases, the sensitivity becomes higher. The maximum sensitivity was obtained via calculation, which was 2200 nm/RIU when R_1 was

240 nm, and the maximum FOM was 47.8. Thus, in practical applications, the radius R_1 should be appropriately increased to obtain a better sensing performance.

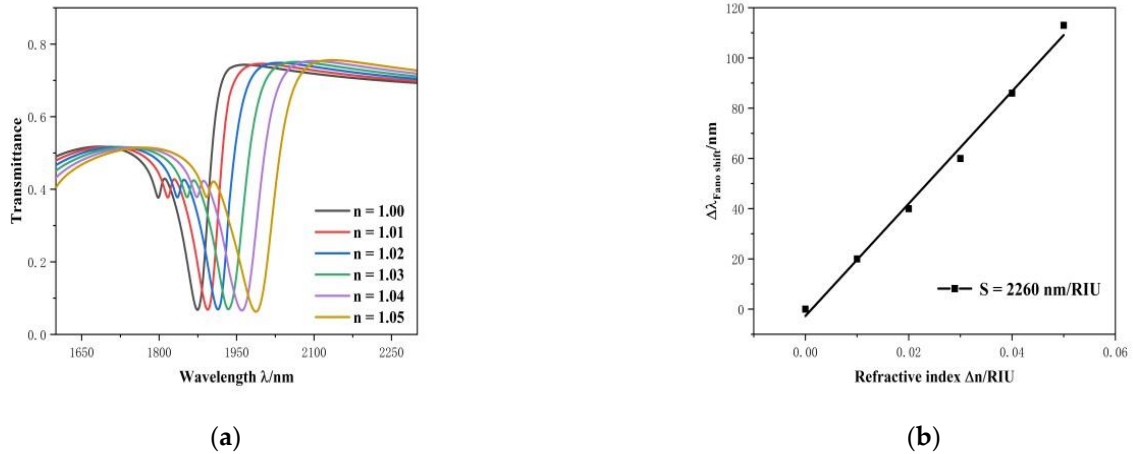


Figure 4. (a) Transmission spectrum of the whole system for various refractive indexes; (b) variation of the dip point's wavelength in Fano resonance ($\Delta\lambda$) with a changed refractive-index (Δn).

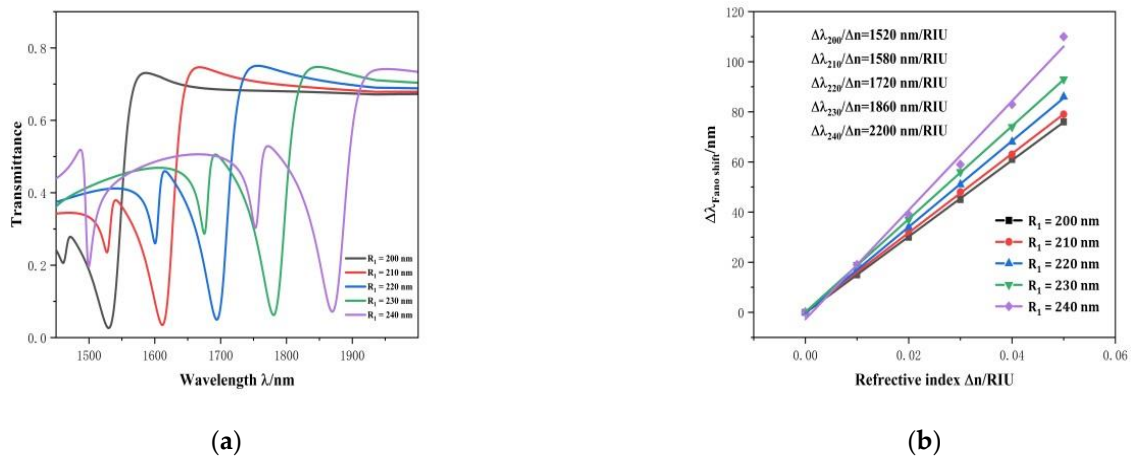


Figure 5. (a) Transmission spectrum of the outer ring of CCDRR for different external radii R_1 ; (b) shifts of the dip point in Fano resonance ($\Delta\lambda$) with a changed refractive-index (Δn).

The effects of different external radii R_2 of the inner ring of the CCDRR on the transmission capabilities were investigated as 90, 100, 110, 120, and 130 nm, while setting the parameter value R_1 as 240 nm and keeping the other parameters the same. As shown in Figure 6a, the dip wavelength of Fano resonance was almost constant. When R_2 increases, the dip point of Fano resonance has a slight red-shift and the transmittance of the dip marginally decreases, and there is a slight increase in sensitivity, which is described in Figure 6b. When $R_2 = 130$ nm, the sensitivity of the structure attained the highest value: 2260 nm/RIU with a FOM of 56.5.

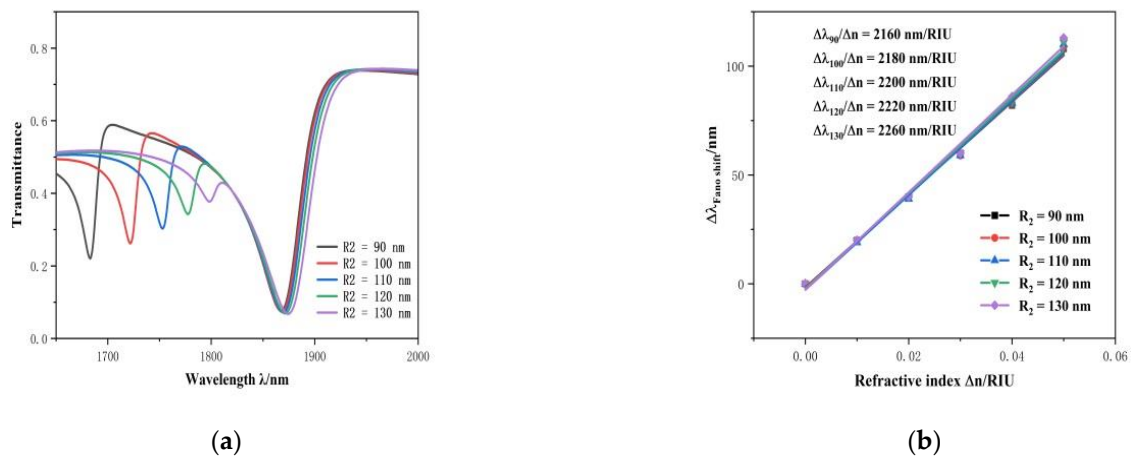


Figure 6. (a) Transmission spectra of the inner ring of CCDRR for different external radii R_2 ; (b) shifts of the dip point in Fano resonance ($\Delta\lambda$) with a changed refractive-index (Δn).

Afterward, the effect of the separation H of the two symmetric rectangular baffles on the propagation performance was studied. The transmission spectra that are displayed in Figure 7a were calculated at different separations for $H = 540, 560, 580, 600,$ and 620 nm, while the other geometric parameters were kept the same. It was found that no matter how H changed, the dip wavelength of Fano resonance remained almost unchanged, though the FOM obviously decreased, as represented in Figure 7b. There was an optimal simulation result: the sensitivity was 2260 nm/RIU and FOM was 56.5 . Then, the other geometric parameters were kept the same, except for increasing the height of the rectangular baffle h from 130 to 170 nm in steps of 10 nm. The transmission spectra and the change of FOM of the diverse heights of the rectangle baffles are shown in Figure 7c,d, respectively. As shown in Figure 7c, with the increase of h , the dip wavelength only demonstrates a slight blue-shift, while the Fano line shape changes significantly. According to the calculation, when $h = 150$ nm, the maximum sensitivity is 2260 nm/RIU with a FOM of 56.5 . As h continues to increase, the sensitivity will decrease as well as the FOM.

The separation of the two symmetrical rectangular baffles H and the heights of the two baffles h are pivotal to the waveguide with two rectangle baffles. According to the simulation results, the successive wide-band mode has a significant effect on the line shape of Fano resonance, but not on the wavelength of the dip point.

To further investigate the effects of the coupling gap between the CCDRR and the waveguide on the propagation properties, g was increased from 10 nm to 30 nm while the other geometric arguments were fixed at $R_1 = 240$ nm, $R_2 = 130$ nm, $H = 540$ nm, and $h = 150$ nm. The transmission performances of the structure with different coupling gaps between the CCDRR and the waveguide for $g = 10, 15, 20, 25,$ and 30 nm can be seen in Figure 8a. With increasing g , the dip wavelength of the Fano resonance shows a blue-shift, the FWHM tends to narrow and the transmittance of the dip position of Fano resonance tends to move higher. The fact that the coupling intensity weakens as the coupling gap increases can account for this phenomenon. Additionally, the sensitivity of the system decreased with the increase of g , as shown in Figure 8b. Thus, the optimal performance parameters can be obtained when the sensitivity is 2260 nm/RIU and the FOM is 56.5 .

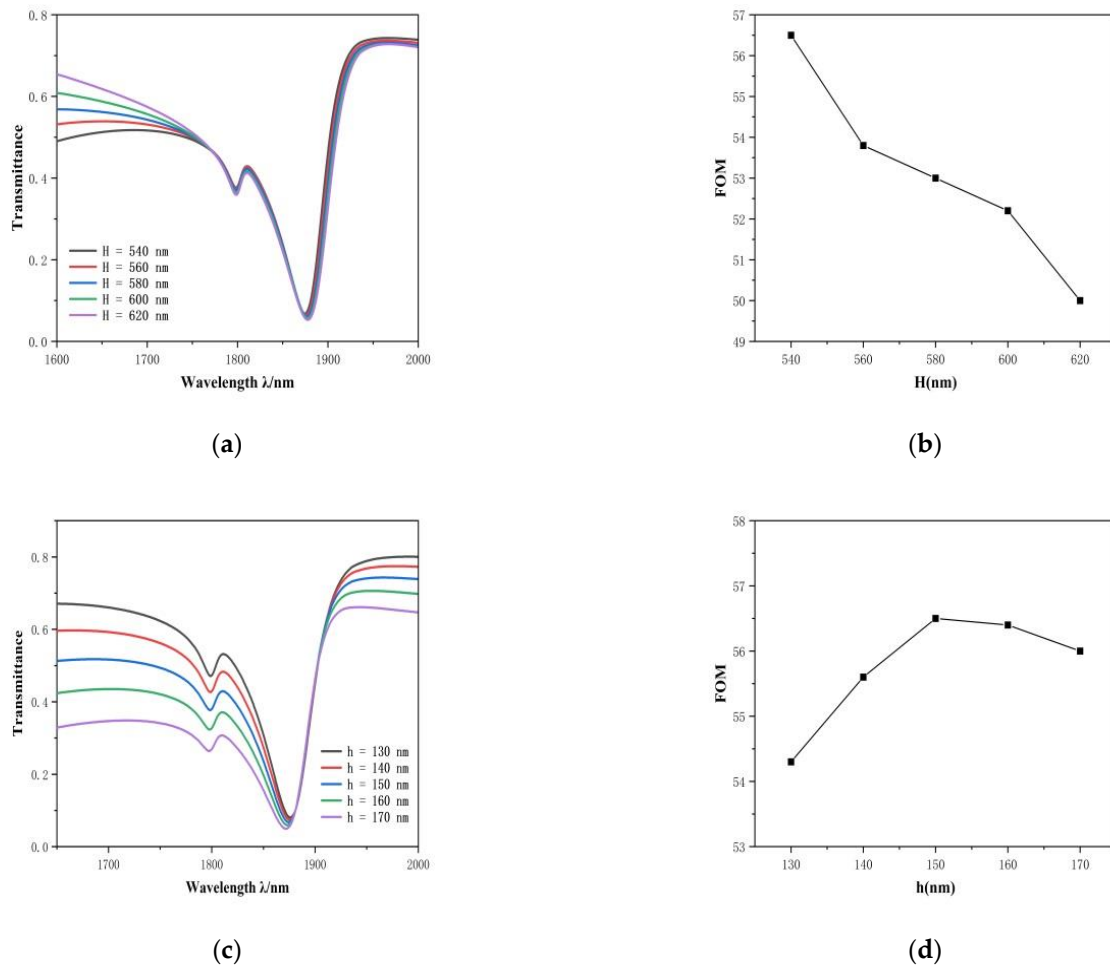


Figure 7. (a) Transmission spectra for the different separations H of the twin symmetrical rectangular baffles; (b) varying figure of merit (FOM) with increasing separation between the two rectangular baffles; (c) transmission spectra for the various heights of the two symmetrical rectangular baffles; and (d) varying FOM with increasing height of the two rectangular baffles.

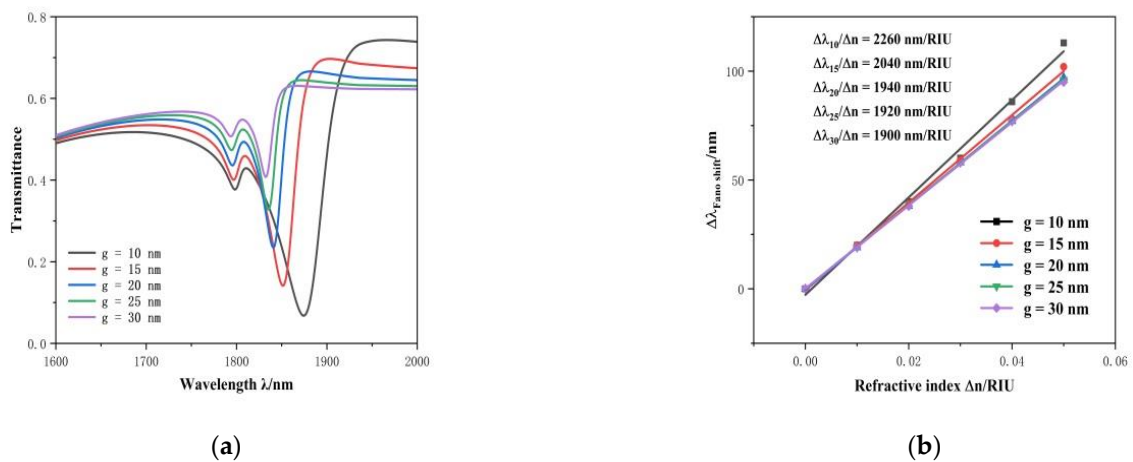


Figure 8. (a) Transmission spectra for various coupling gaps g between the CCDRR and waveguide; (b) shifts of the dip point in Fano resonance ($\Delta\lambda$) with a changed refractive-index (Δn).

4. Application of the Proposed Structure in Temperature Sensing

The presented system can also be used as a nanoscale temperature sensor, which is realized by using the variation of the refractive indices of the temperature sensing medium caused by an ambient temperature, with the temperature sensing material viewed as a liquid. Ethanol was chosen as the temperature sensing medium to fill the CCDRR and the MIM waveguide with a bus waveguide and two symmetrical rectangular baffles because of its high refractive-index temperature parameter of $3.94 \times 10^{-4} (\text{°C}^{-1})$. The refractive-index temperature coefficients of Ag and quartz are $9.30 \times 10^{-6} (\text{°C}^{-1})$ and $8.60 \times 10^{-6} (\text{°C}^{-1})$, respectively, which are two orders of magnitude smaller than that of ethanol. Thus, the variation of temperature largely affects ethanol, and the effects of thermal expansion of Ag and quartz can be ignored. The schematic diagram of three-dimensional (3D) structure is shown in Figure 9. The blue part represents ethanol, the green part represents silver, and the black part represents the quartz substrate.

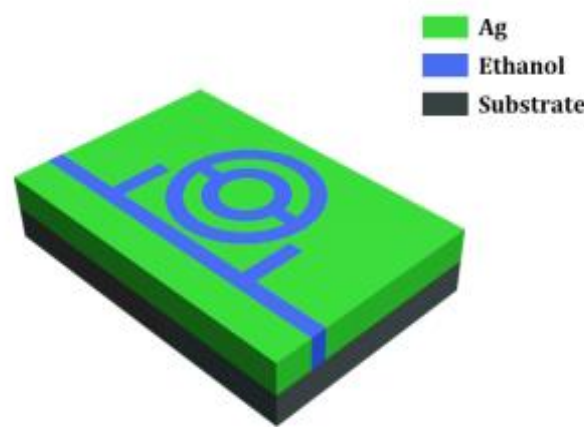


Figure 9. Three-dimensional schematic of the temperature sensor based on the MIM waveguides.

Commonly, the functional connection between the refractive index, temperature coefficient, and ambient temperature of a liquid temperature sensing material can be expressed as follows [36]:

$$n = n_0 + \frac{dn}{dT} (T - T_0) \quad (7)$$

where $n_0 = 1.36048$ is the refractive index of the liquid corresponding to room-temperature, $T_0 = 20 \text{ °C}$; $dn/dT = 3.94 \times 10^{-4} (\text{°C}^{-1})$ is the refractive index temperature coefficient; and T represents the ambient temperature. Thus, the refractive index formula, with ethanol as the filling material of the temperature sensor, and the sensitivity formula can be expressed as follows:

$$n = 1.36048 - 3.94 \times 10^{-4} (T - 20) \quad (8)$$

$$S_T = \frac{\Delta \lambda_T}{\Delta T} \quad (9)$$

The geometric arguments of the structure were fixed at $R_1 = 240 \text{ nm}$, $R_2 = 130 \text{ nm}$, $d = 40 \text{ nm}$, $H = 540 \text{ nm}$, $h = 150 \text{ nm}$, $g = 10 \text{ nm}$, and $w = 50 \text{ nm}$. The transmission spectrum for the disparate temperatures of the sensor is plotted in Figure 10a. As the melting and boiling points of ethanol are -144.3 °C and 78.4 °C , respectively, the temperature sensor has good stability in the working range of -80 – 60 °C . As the temperature drops from 60 °C to -80 °C with an interval of 20 °C , the transmission spectrum displays a red-shift phenomenon and the sensitivity, which is shown as Figure 10b, has a remarkable linear fit with the value of 1.48 nm/°C .

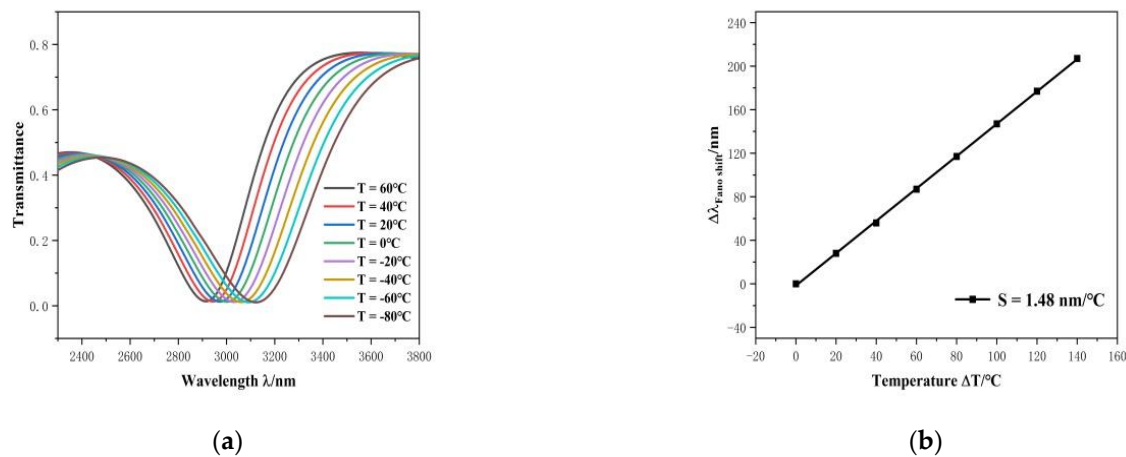


Figure 10. (a) Transmission spectrum for the disparate temperatures of the sensor; (b) shifts of the dip point in Fano resonance ($\Delta\lambda_T$) with a changed temperature (ΔT).

Although the temperature sensor has some advantages, such as a high sensitivity, a simple structure, and easy integration, it still has some limitations. Due to the bounds of the boiling and melting points of ethanol, the sensor is only suitable for low-temperature sensing, and it cannot solve sensing problems when the temperature is too high. As a liquid substance, ethanol cannot meet the needs of solid-state sensing equipment under some special conditions. In some practical applications, thermal materials such as lithium niobate can be used instead of ethanol to manufacture solid-state equipment. In future research, we will also consider adding a graphene strip into the CCDRR cavity to allow for dynamic adjustment of the sensitivity.

5. Conclusions

In this work, a plasmonic refractive-index nano-sensor consisting of MIM waveguides with two symmetrical rectangular baffles, coupled with a connected concentric double rings resonator (CCDRR), has been devised, and its transmission characteristics have been studied by introducing the finite element method (FEM). The transmission spectrum of the structure showed an asymmetric and sharp shape, due to Fano resonance caused by the destructive interference between the successive wide-band mode of the two rectangular baffles on the bus waveguide and the discontinuous narrow-band mode of the CCDRR. We then analyzed the effects of the refractive index and geometric arguments on the transmission performance levels of the structure. With increases of the refractive index n , external radii of the outer circular ring R_1 , and the inner circular ring R_2 , the dip point of Fano resonance showed a red shift, while with increases of coupling gap g , the dip wavelength showed a blue shift. Changes to the separation between the two rectangular baffles H and to the heights of the two baffles h had a significant effect on the line shape of Fano resonance, but not on the wavelength of the dip. The designed structure achieved an optimal performance when the structural parameters were as follows: $R_1 = 240 \text{ nm}$, $R_2 = 130 \text{ nm}$, $H = 540 \text{ nm}$, $h = 150 \text{ nm}$, and $g = 10 \text{ nm}$. The sensitivity of the proposed sensor could reach $2260 \text{ nm}/\text{RIU}$ with a high FOM of 56.5. Finally, its application in the temperature sensor field with ethanol instead of air was also studied, and the sensitivity was finetuned to $1.48 \text{ nm}/^\circ\text{C}$. The designed structure has good application prospects in temperature sensors and other photonic devices.

Author Contributions: Conceptualization, S.Y. and P.L.; methodology, P.L. and X.W.; software, P.L.; validation, S.Y., X.Z., and T.L.; formal analysis, X.Z. and Y.R.; investigation, T.L.; data curation, X.W. and E.H.; writing—original draft preparation, P.L.; writing—review and editing, Y.R., X.Z., and T.L.; supervision, S.Y. and L.S. All authors have read and agreed to the published version of the manuscript.

Funding: This work was supported in part by the National Natural Science Foundation of China, under grants 61875250 and 61975189; in part by the Zhejiang Provincial Natural Science Foundation of China, under grant LD21F050001; and in part by the Key Research and Development Project of Zhejiang Province, under grant 2021C03019.

Conflicts of Interest: The authors declare no conflict of interest.

References

1. Barnes, W.L.; Dereux, A.; Ebbesen, T.W. Surface plasmon subwavelength optics. *Nature* **2003**, *424*, 824–830. [[CrossRef](#)] [[PubMed](#)]
2. Gramotnev, D.K.; Bozhevolnyi, S.I. Plasmonics beyond the diffraction limit. *Nat. Photonics* **2010**, *4*, 83–91. [[CrossRef](#)]
3. Yin, Y.; Qiu, T.; Li, J.; Chu, P.K. Plasmonic nano-lasers. *Nano Energy* **2012**, *1*, 25–41. [[CrossRef](#)]
4. Lezec, H.J.; Degiron, A.; Devaux, E.; Linke, R.A.; Martin-Moreno, L.; Garcia-Vidal, F.J.; Ebbesen, T.W. Beaming light from a subwavelength aperture. *Science* **2002**, *597*, 820–822. [[CrossRef](#)] [[PubMed](#)]
5. Weiner, J. The electromagnetics of light transmission through subwavelength slits in metallic films. *Opt. Express* **2011**, *19*, 16139–16153. [[CrossRef](#)] [[PubMed](#)]
6. Kekatpure, R.D.; Barnard, E.S.; Cai, W.; Brongersma, M.L. Phase-coupled plasmon-induced transparency. *Phys. Rev. Lett.* **2010**, *104*, 243902. [[CrossRef](#)] [[PubMed](#)]
7. Yan, S.; Zhang, M.; Zhao, X.; Zhang, Y.; Wang, J.; Jin, W. Refractive index sensor based on a metal–insulator–metal waveguide coupled with a symmetric structure. *Sensors* **2017**, *17*, 2879. [[CrossRef](#)]
8. Yang, X.Y.; Hua, E.T.; Su, H.; Guo, J.; Yan, S.B. A nanostructure with defect based on Fano resonance for application on refractive-index and temperature sensing. *Sensors* **2020**, *20*, 4125. [[CrossRef](#)] [[PubMed](#)]
9. Qiao, L.T.; Zhang, G.M.; Wang, Z.S.; Fan, G.P.; Yan, Y.F. Study on the Fano resonance of coupling M-type cavity based on surface plasmon polaritons. *Opt. Commun.* **2019**, *433*, 144–149. [[CrossRef](#)]
10. Limonov, M.F.; Rybin, M.V.; Poddubny, A.N.; Kivshar, Y.S. Fano resonance in photonics. *Nat. Photonics* **2017**, *11*, 543–554. [[CrossRef](#)]
11. Chen, J.; Gan, F.; Wang, Y.; Li, G. Plasmonic sensing and modulation based on Fano resonances. *Adv. Opt. Mater.* **2018**, *6*, 1701152. [[CrossRef](#)]
12. Huang, C.Y.; Chang, H.C. Plasmon coupling within the multifold nanorod metasurface for sensing applications. *IEEE Photonics J.* **2019**, *11*, 1–8. [[CrossRef](#)]
13. Du, C.L.; Yang, W.C.; Peng, S.; Shi, D.N. Optimal geometry parameter for plasmonic sensitivities of individual Au nanoparticle sensors. *Phys. Chem. Chem. Phys.* **2019**, *21*, 7654–7660. [[CrossRef](#)] [[PubMed](#)]
14. Wu, C.; Khanikaev, A.B.; Shvets, G. Broadband slow light metamaterial based on a Double-Continuum Fano resonance. *Phys. Rev. Lett.* **2011**, *106*, 107403. [[CrossRef](#)] [[PubMed](#)]
15. Chang, W.S.; Lassiter, J.B.; Swanglap, P.; Sobhani, H.; Khatua, S.; Nordlander, P.; Halas, N.J.; Link, S. A plasmonic Fano switch. *Nano Lett.* **2012**, *12*, 4977–4982. [[CrossRef](#)]
16. Lu, H.; Wang, G.X.; Liu, X.M. Manipulation of light in MIM plasmonic waveguide systems. *Chin. Sci. Bull.* **2013**, *58*, 3607–3616. [[CrossRef](#)]
17. Park, J.; Kim, K.Y.; Lee, I.M.; Na, H.; Lee, S.Y.; Lee, B. Trapping light in plasmonic waveguides. *Opt. Express* **2010**, *18*, 598–623. [[CrossRef](#)]
18. Novikov, I.V.; Maradudin, A.A. Channel polaritons. *Phys. Rev. B* **2002**, *66*, 035403. [[CrossRef](#)]
19. Smith, C.L.C.; Stenger, N.; Kristensen, A.; Mortensen, N.A.; Bozhevolnyi, S.I. Gap and channeled plasmons in tapered grooves: A review. *Nanoscale* **2015**, *7*, 9355–9386. [[CrossRef](#)] [[PubMed](#)]
20. Willingham, B.; Link, S. Energy transport in metal nanoparticle chains via sub-radiant plasmon modes. *Opt. Express* **2011**, *19*, 6450–6461. [[CrossRef](#)]
21. Amini, A.; Aghili, S.; Golmohammadi, S.; Gasemi, P. Design of microelectromechanically tunable metal–insulator–metal plasmonic band-pass/stop filter based on slit waveguides. *Opt. Commun.* **2017**, *403*, 226–233. [[CrossRef](#)]
22. Yang, X.Y.; Hua, E.T.; Wang, M.M.; Wang, Y.F.; Wen, F.; Yan, S.B. Fano resonance in a MIM waveguide with two triangle stubs coupled with a split-ring nanocavity for sensing application. *Sensors* **2019**, *19*, 4972. [[CrossRef](#)]
23. Tang, Y.; Zhang, Z.D.; Wang, R.B.; Hai, Z.Y.; Xue, C.Y.; Zhang, W.D.; Yan, S.B. Refractive index sensor based on Fano resonances in metal-insulator-metal waveguides coupled with resonators. *Sensors* **2017**, *17*, 784. [[CrossRef](#)] [[PubMed](#)]
24. Su, H.; Yan, S.B.; Yang, X.Y.; Guo, J.; Wang, J.X.; Hua, E.T. Sensing Features of the Fano Resonance in an MIM Waveguide Coupled with an Elliptical Ring Resonant Cavity. *Appl. Sci.* **2020**, *10*, 5096. [[CrossRef](#)]
25. Hwang, Y.; Kim, J.E.; Park, H.Y. Frequency selective metal-insulator-metal splitters for surface plasmons. *Opt. Commun.* **2011**, *284*, 4778–4781. [[CrossRef](#)]
26. Chen, J.; Li, Z.; Lei, M.; Fu, X.; Xiao, J.; Gong, Q. Plasmonic Y-splitters of high wavelength resolution based on strongly coupled-resonator effects. *Plasmonics* **2011**, *7*, 441–445. [[CrossRef](#)]
27. Ma, F.; Lee, C. Optical nanofilters based on meta-atom side-coupled plasmonics metal-insulator-metal waveguides. *J. Lightwave Technol.* **2013**, *31*, 2876–2880. [[CrossRef](#)]
28. Wang, S.; Li, Y.; Xu, Q.; Li, S. A MIM filter based on a side-coupled crossbeam square-ring resonator. *Plasmonics* **2016**, *11*, 1291–1296. [[CrossRef](#)]

29. Han, Z.; Forsberg, E.; He, S. Surface plasmon Bragg gratings formed in metal–insulator–metal waveguides. *IEEE Photonics Technol. Lett.* **2007**, *19*, 91–93. [[CrossRef](#)]
30. Par, J.; Kim, H.; Lee, B. High order plasmonic Bragg reflection in the metal–insulator–metal waveguide Bragg grating. *Opt. Express* **2008**, *16*, 413–425.
31. Gai, H.; Wang, J.; Tian, Q. Modified Debye model parameters of metals applicable for broadband calculations. *Appl. Opt.* **2007**, *46*, 2229–2233. [[CrossRef](#)] [[PubMed](#)]
32. Kekatpure, R.D.; Hryciw, A.C.; Barnard, E.S.; Brongersma, M.L. Solving dielectric and plasmonic waveguide dispersion relations on a pocket calculator. *Opt. Express* **2009**, *17*, 24112–24129. [[CrossRef](#)] [[PubMed](#)]
33. Zhu, J.H.; Wang, Q.J.; Shum, P.; Huang, X.G. A simple nanometric plasmonic narrow-band filter structure based on metal-insulator-metal waveguide. *IEEE Trans. Nanotechnol.* **2011**, *10*, 1371–1376. [[CrossRef](#)]
34. Hu, F.; Yi, H.; Zhou, Z. Wavelength demultiplexing structure based on arrayed plasmonic slot cavities. *Opt. Lett.* **2011**, *36*, 1500–1502. [[CrossRef](#)] [[PubMed](#)]
35. Mayer, K.M.; Hafner, J.H. Localized surface plasmon resonance sensors. *Chem. Rev.* **2011**, *111*, 3828–3857. [[CrossRef](#)] [[PubMed](#)]
36. Peng, Y.; Hou, J.; Huang, Z.; Lu, Q. Temperature sensor based on surface plasmon resonance within selectively coated photonic crystal fiber. *Appl. Opt.* **2012**, *51*, 6361–6367. [[CrossRef](#)] [[PubMed](#)]